UC Santa Cruz
UC Santa Cruz Electronic Theses and Dissertations

Title

Non-invasive Imaging of Gut Derived Neuromodulation in Fly by Three-photon Microscopy

Permalink

https://escholarship.org/uc/item/8qs4d9gd

Author

Hossain, Golam Md Imran

Publication Date

2020

Peer reviewed|Thesis/dissertation

UNIVERSITY OF CALIFORNIA

SANTA CRUZ

NON-INVASIVE IMAGING OF GUT DERIVED NEUROMODULATION IN FLY BY THREE-PHOTON MICROSCOPY

A dissertation submitted in partial satisfaction
of the requirements for the degree of

DOCTOR OF PHILOSOPHY

in

ELECTRICAL ENGINEERING

by

Golam Md. Imran Hossain

June 2020

The Dissertation of Golam Md. Imran
Hossain is approved:

_____
Professor Marco Rolandi, Chair

_____
Professor Jing W. Wang

_____
Professor Yi Zuo

_____
Professor Sara Abrahamsson

_____
Quentin Williams
Acting Vice Provost and Dean of Graduate Studies

Table of Contents

List of Figures

Abstract

Golam Md. Imran Hossain

Non-invasive imaging of gut derived neuromodulation
in fly by three-photon microscopy

A variety of *in vivo* imaging techniques have been invented and adopted to study brain function, giving us unprecedented access to dynamics of neuronal circuits from single synapse to large scale network activity. Three-photon microscopy is one of the latest additions, primarily developed for imaging deeper into the brain, and it has shown promises in probing neuronal circuits of an intact animal through highly scattering exoskeleton with minimal or no surgery in mouse, adult zebrafish and fly. Among the model organisms, the fruit fly – *Drosophila*, has the most comprehensive genetic toolkit, and only the second organism after *Caenorhabditis elegans* to have a mapped out connectome. The fly brain, with a modest number of neurons (135,000), supports a repertoire of complex behaviors that have been quantitatively studied in laboratories for decades. Reduced complexity, genetic tractability, and the blueprint of neuronal connections make the fly brain is an attractive system to study the neural basis of behavior. The nervous system integrates external stimuli and internal states such as motivation, arousal, drive or emotion to drive adaptive behavior. Hormones and neuromodulators encode internal states and exert influence by modulating or reconfiguring neuronal circuits to shape behavior. Typical *in vivo* imaging in fly requires removing the cuticle to create an optical window, which perturbs the hormones in the fly's open circulatory system. Here I describe the construction of a three-photon microscope for transcuticle imaging of the fly brain with an emphasis on optimum photon collection. Next, using this noninvasive imaging system, I show how a gut-derived neuropeptide hormone travels through the circulation, modulates a brain circuit, and switches male fly behavior from feeding to mating.

1   Introduction

1.1   Multiphoton scanning microscopy

Confocal microscopy (single-photon laser scanning microscopy) is limited to imaging at the superficial layers of a scattering tissue. Confocal pinhole rejects out of focus emission to achieve optical sectioning. However, when the emission photons from the image plane get progressively scattered with depth in a turbid tissue, photon collection through pinhole drops according. For example, *in vivo* brain imaging is only possible down to ~150 μm in the mouse cortex using a confocal microscope (Takahara, Matsuki and Ikegaya, 2011). Two-photon excitation microscopy adapts a couple of strategies to extend the imaging depth. First, two-photon excitation microscopy uses longer excitation wavelengths that are less susceptible to scattering. Second, the optical sectioning is achieved by the nonlinear confinement of absorption in the perifocal region (Denk, Strickler and Webb, 1990; Theer and Denk, 2006). This allows a two-photon excitation microscope to collect both ballistic and scattered photons. Nevertheless, the imaging depth of two-photon excitation microscopy is limited by the signal-to-background ratio (SBR). At a certain depth, SBR becomes unity when the surface layers of the tissue generate the same amount of signal as the ballistic photons at the focus (Theer and Denk, 2006). For mouse cortex, the SBR drops to 1 at the depth of 500 μm in a typical two-photon microscopy setup.

The imaging depth can be further improved by suppressing the background excitation with third-order absorption – three-photon excitation microscopy. Hell et al. demonstrated the feasibility of three-photon excitation to scanning fluorescence microscopy in 1996 (Hell, 1996) using polystyrene beads stained with fluorophore 2,5-bis(4-biphenyl) oxazole. Wokosin et al. applied three-photon excitation microscopy for *in vivo* imaging of DNA undergoing mitosis from metaphase through telophase in a LLC-PK cell (Wokosin *et al.*, 1996).

More recently, a new class of light source enabled *in vivo* three-photon excitation microscopy in the mouse brain with a genetically encoded fluorescent reporter (RFP) (Horton *et al.*, 2013). In addition to fluorescent imaging, the high energy excitation beam of a multiphoton microscope interacts with intrinsic indicators such as collagen and microtubules to generate optical harmonic generation (second-harmonic generation: SHG and third-harmonic generation: THG)(Zipfel *et al.*, 2003). These optical harmonic generation signals are a complementary label-free imaging modality to fluorescent imaging.

In multiphoton fluorescence microscopy, fluorescent molecules absorb multiple photons (usually two/three photons) simultaneously (within $\sim 10^{-16}$ s) to transition from ground states to excited states. As the excited fluorescent molecules relax to the ground state by radiative decay of a single photon, this emitted photon is blue-shifted compare to the excitation photons (Figure 1.1)

1.1.1 Second-harmonic generation and third-harmonic generation

Unlike multiphoton excited fluorescence, SHG and THG are elastic scatter process where the emitted photon has the energy equal to the sum of excitation photons. During optical harmonic generation, the light-matter interaction leaves the quantum states of the materials unchanged and the transition is described as a quantum jump to a virtual state. Structures without inversion symmetry such as collagen and microtubules generate strong SHG signal (Freund and Deutsch, 1986; Zipfel *et al.*, 2003), while all materials with non-zero third-order susceptibility, interface with different refractive indices are strong sources of THG (Barad *et al.*, 1997). The difference between multiphoton and SHG/THG is illustrated in figure 1.1.
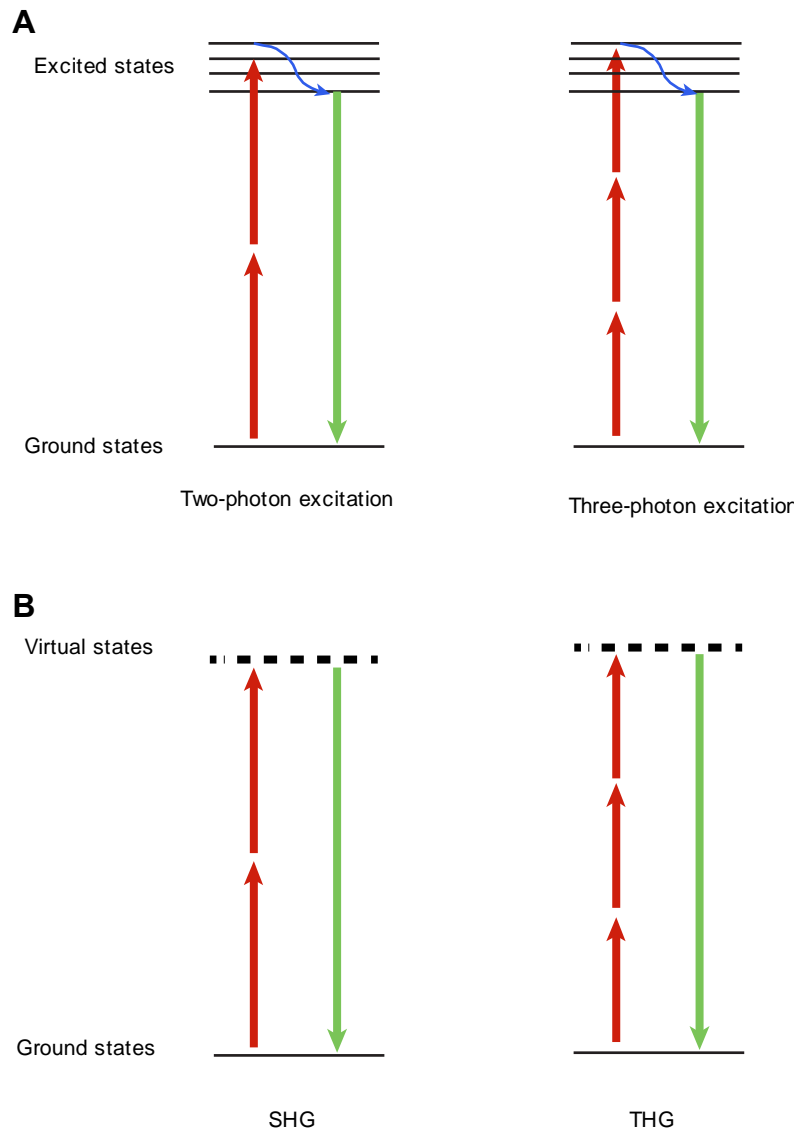
Figure 1.1 Multiphoton modalities.

Energy diagram: (A) Two-photon excitation and three-photon excitation. (B) Second-harmonic generation (SHG) and third-harmonic generation (THG). Solid lines representing real energy states, dashed lines representing virtual energy states.

1.2 Extending imaging depth into scattering tissue

Scattering limits the ability of the optics to form a sharp focus inside a tissue – which drops exponentially with the depth (Helmchen and Denk, 2005). One strategy to extend imaging depth into a turbid tissue is by using higher energy pulses that results in more photons reaching the excitation volume at deeper tissue depths, while reducing the average power (reducing the duty cycle of the laser) below the damage threshold of the sample. Theer et al. successfully imaged the mouse cortex at a depth of 1,000 µm using a 925-nm laser source of 3 µJ per pulse and a repetition rate of 200 kHz (Theer, Hasan and Denk, 2003). Another strategy to extend imaging depth is to use a longer excitation wavelength to reduce tissue scattering. Kobat et al. reached an imaging depth of 1.6 mm in mouse brain using 1,280 nm excitation light with 1.5 nJ pulse energy and a repetition rate of 80 MHz (Kobat, Horton and Xu, 2011).

However, when using longer wavelength excitation at near-infrared spectral regime, water absorption in the tissue becomes a dominant factor. Thus the optimum wavelength window for imaging the mouse cortex is a trade-off between tissue scattering and tissue absorption [Horton, *Nature photonics* 2013]. This combined effect of absorption and scattering can be represented by effective attenuation length (l_e), a harmonic mean of the attenuation length due to water absorption (l_a) and the attenuation length due to scattering (l_s). Thus, $l_e = (1/l_a + 1/l_s)^{-1}$. Figure 1.2 plots l_e, l_a and l_s against wavelength for the mouse cortex (Kou, Labrie and Chylek, 1993) (Theer, Hasan and Denk, 2003; Kobat *et al.*, 2009). Two optimum imaging windows in terms of tissue penetration near 1,300 nm and 1,700 nm clearly emerges for this analysis and has been experimentally validated recently (Wang *et al.*, 2018). The 1,300 nm and 1,700 nm imaging would be referred to as green and red imaging window from this point onwards for brevity. Combining long wavelength excitation and high energy excitation, Horton et al. demonstrated three-photon fluorescence imaging at a depth of 1.4 mm with 1,700 nm excitation and 67 nJ laser pulse (1 MHz repetition rate) (Horton *et al.*, 2013). Moreover, three-photon

absorption spectrums of currently available genetically encoded fluorescent proteins (green fluorescent protein, GFP and red fluorescent protein, RFP) and their calcium reporter variants – GCaMP and RCaMP overlap with these 1,300 and 1,700 nm imaging windows, respectively (Figure 1.2 B).

A

B

	1P	2P	3P
GCaMP	495 nm	930 nm	1,320 nm
RCaMP	520 nm	1,070nm	1,650 nm
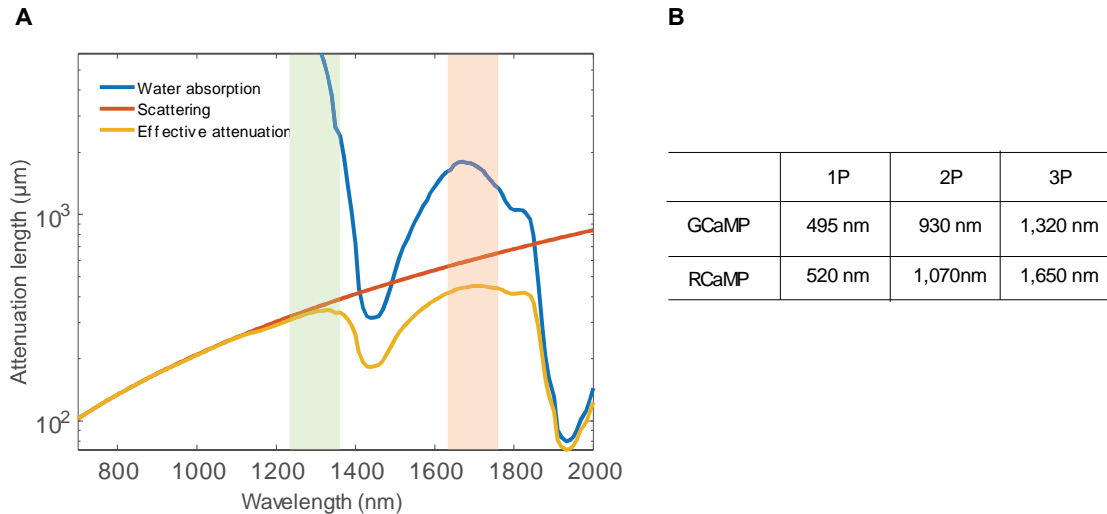
Figure 1.2 Three-photon imaging window.

(A) Scattering limited attenuation length, water absorption limited attenuation length and effective attenuation length in mouse cortex. (B) Peak excitation wavelengths of genetically encoded calcium indicator for single-photon and multiphoton excitation.

Another reason the three-photon fluorescent microscopy outshines two-photon excitation microscopy for deep imaging is its better three-dimensional localization with a higher (3rd) order of nonlinearity. The requirement of simultaneous absorption of three photons gives rise to the relation of a signal proportional to the light intensity cubic: $F_{3P} \propto I^3$, where F_{3P} is the fluorescence signal in three-photon fluorescent microscopy, I is the excitation light intensity. Whereas in two-photon fluorescent microscopy, fluorescence is proportional to the light intensity squared, $F_{2P} \propto I^2$. As a result, the fluorescence signal of three-photon absorption falls off as $\sim 1/z^4$ (where z

is the distance away from the focal plane), while the fluorescence of two-photon absorption falls off as ~ $1/z_2$ (Xu *et al.*, 1996). Therefore, three-photon absorption dramatically reduces the out-of-focus background in regions far away from the focal plane, improving the SBR compared to two-photon excitation.

1.3   Challenges of imaging fly brain

Insects wear their skeleton outside their body, a mechanical armor made out of cuticle, providing protection and mechanical stability and often decorated with pigments. Organs reside inside this body cavity forged by the exoskeleton submerged in hemolymph – the insect equivalent of blood. A contractile dorsal longitudinal vessel, the heart equivalent, keeps the hemolymph in motion inside the body cavity, forming an open circulatory system. However, hemolymph does not play a part in the transport of oxygen and other gases. Instead, an elaborate network of tracheal tubules, extending to all parts of the body, carry oxygen directly to the site of use. All these adaptations by insects make it challenging to image the fly brain in action, especially in its native state.   Current methods optical imaging of fly brain require removal of the body armor (cuticle) over the head, as well as air sacs, trachea, fat body and other connective tissue underneath the cuticle to gain optical access to the nervous system (Huang *et al.*, 2018). Even with clear optical access to the brain, imaging through the entire fly brain — roughly the size of a poppy seed — is an ordeal, due to formidable scattering from the air-filled tracheal network, arborizing across the brain (Hsu *et al.*, no date). And the surgical removal of a piece of cuticle for imaging compromises the integrity of the circulatory system, preventing one from probing the interplay of the nervous system with other organs through circulation. Transcuticle imaging by three-photon microscopy in the fly, give us access to investigating such coordination.

1.4   Remarks

There is no single best imaging method for addressing all biological questions; an imaging technology, despite its many short comings, may be best suited for a specific biological application. Three-photon microscopy offers capability for imaging intact animals through their highly scattering tissue (e.g., cuticle, skull). In the following chapters I will discuss the construction of a three-photon microscope with optimum post-objective collection and application of three-photon microscopy for non-invasive visualization of neuromodulation in the fly brain.

2 Design of a Three-Photon Microscope Optimized for Fly Brain Imaging

Three-photon microscopy allows *in vivo* imaging through highly scattering tissue (T. Wang et al., 2018). However, due to low three-photon absorption cross-section; high-energy and ultrashort laser pulses are required for three-photon imaging. Considering the minute size of a fly, near-optimal imaging is warranted. This requires optimizing the excitation light, as well as maximizing the collection of the emission. In this chapter, I describe a custom-built three-photon microscope with optimized excitation and collection for imaging the fly brain in both green and red imaging window.

2.1 Excitation source

Multiphoton microscopy relies on 'simultaneous' (within ~0.5 fs) interaction of multiple (two/three) photons with an optically active species (fluorophores), requiring a high photon density supplied by ultrafast lasers (W Denk et al., 1990; Helmchen & Denk, 2005). The interaction probability depends on the physical properties of the optically active species – multiphoton absorption cross-section, and the fluorescence emission strength depends on the quantum efficiency of the fluorophore. An average excitation power, $<P>$, in a transparent sample and at the paraxial limits, generates F_{gen} fluorescent photons per fluorophore per unit time. F_{gen} can be expressed as:

$$F_{gen} \approx \eta \frac{\sigma}{\tau^{n-1}R^2} \left(\frac{NA^2}{2\hbar c \lambda} \right)^n \langle P \rangle^n \qquad ...(2.1)$$

where η, σ, τ, n and R are the fluorophore quantum efficiency, absorption cross-section, laser pulse duration, order of fluorescent absorption (2 and 3 for two-photon and three-photon events, respectively) and pulse repetition rate, respectively. NA is the objective numerical aperture, $\hbar$ is reduced Planck's constant, and the excitation wavelength is λ (W Denk et al.,

1990). The cross-section of a typical fluorophore for the three-photon absorption ($\sim 10^{-82}$ cm^{6}s^2/photon) is orders of magnitude lower than the two-photon absorption cross-section ($\sim 10^{-49}$ cm^{4}s/photon) (Xu et al., 1996). However, the fluorescent signal and the duty cycle of the pulse train follows an inverse-squared relationship for the three-photon microscope, as opposed to the simple inverse relationship for the two-photon microscopy (equation 2.1). This allows three-photon imaging with an ultrashort (< 70 fs) and energetic (~ 0.5-2 nJ) pulses operating at a low duty cycle (~ 1 MHz) while maintaining an average excitation power comparable to a two-photon imaging system (Horton et al., 2013).

Ti:Sapphire mode-locked laser – the workhorse light source for two-photon imaging – has a tunable emission ranging from 680 nm to 1,080 nm (Svoboda & Yasuda, 2006) and a repetition rate of ~80 MHz, thus not suitable for three-photon imaging of typical (genetically encoded) fluorophores and calcium activity reports. Moreover, there is no lasing medium that supports emission at the three-photon green (1,300 nm) or red (1,700 nm) imaging window. Thus, the current source for the three-photon imaging is realized by spectral-conversion of mode-locked output form either a Ytterbium-doped laser (1,064 nm) by an Optical Parametric Amplifier (OPA) or Soliton Self-Frequency Shift (SSFS) of an Erbium-doped (1,550 nm) fiber lase by a large diameter photonic-crystal rod (PCR) (Horton et al., 2013; Ouzounov et al., 2017; Yildirim, Sugihara, So, & Sur, 2019).

Here we image fly brains in the green and red window with 1,320 nm and 1,650 nm light, respectively, emitted from an optical parametric amplifier (Opera-F, Coherent) pumped by a 1,035 nm ultrafast laser (1 MHz, 40 W, Monaco, Coherent). The beam is pre-chirped with dispersion compensation unit for maintaining an ultrashort pulse on the imaging plane.

2.2   Movable objective microscope for three-photon imaging

We custom-built a three-photon microscope around a Sutter Movable Objective Microscope (MOM) frame with a pair of 3 mm galvanometric mirrors (6210H, Cambridge Technologies), a 50 mm scan lens (SL50-3P, Thorlabs), a 200 mm tube lens (Nikon), a primary dichroic (cold) mirror (T735LPXRXT-25 × 36, Chroma), a high-NA objective (Olympus XLPLN25XWMP2; 25x 1.05-NA) and two GaAsP photomultiplier tubes (PMT, H11706-40 and H10770B-40, Hamamatsu Photonics).

The emission from the sample is epi-collected and guided towards the detectors by the primary dichroic mirror. Subsequently, the light is separated into the fluorescence and the THG signal by a secondary dichroic beamsplitter (green: Di02-R488-25 × 36, Semrock and red: Di02-R561-25x36, Semrock), housed in a switchable filter cube. Each signal filtered by a band-pass filter. Green fluorescence: a 525 ± 35 nm (ET525/70m-2p, Chroma); red fluorescence: 625 ± 45 nm (FF01-625/90, Semrock); green THG: 445 ± 10 nm (FF01-445/20, Semrock); red THG: 542 ± 13.5 nm (FF01-542/27, Semrock). Three converging lenses interline with these filters guide photons to the detector, the design of which is discussed in section 2.5.

The microscope is controlled by ScanImage 2018b (Vidrio) running on MATLAB 2019a (MathWorks) and a data acquisition module (PXIe-1073NI-5732, PXIe-6341, PXIe-7961, National Instruments). PMT current signal is converted to voltage by a transimpedance amplifier (150 kΩ, 1 MHz low-pass, XPG-ADC-PREAMP, Sigmann Elektronik).

Figure 2.1 shows a schematic of the three-photon microscope. The output beam from the OPA is filtered by a 1,200 nm long-pass filter (FELH1200, Thorlabs) to block residual pump beam. Beam power is attenuated by a combination of an achromatic half-wave plate (AHWP05M-1600, Thorlabs) and a broadband polarizing beamsplitter (PBS054, Thorlabs).

The p-polarized beam out of the attenuator is then pre-chirped with one of the dispersion compensation units and used for imaging. The dispersion of the most optical elements (glass) and immersion fluid (e.g., H_2O and D_2O) is markedly different in the green and red imaging windows. The excitation light exhibits positive dispersion in the green imaging window but anomalous dispersion in the red imaging window. Thus separate dispersion compensation schemes are required for imaging in these two windows. A movable mirror (MM) guides the beam to either of the dispersion compensator units and the beam paths are again merged by a recombining beamsplitter (DM1, DMSP1500, Thorlabs) afterwards. Imaging is done at a reduced excitation NA to minimize scattering by matching the beam diameter to ~ 70% of the objective back aperture. For this, the dispersion compensated beam is demagnified 2 times on the shared optical path, while the 1,320 nm beam is demagnified an additional of 2 times before the paths merge through Keplerian telescopes (AC254-75-C; AC254-150-C, Thorlabs).

2.3   Pre-chirping the excitation beam

Three-photon fluorescence signal strongly depends on the spatio-temporal distribution of the excitation pulse and follows an inverse-squared relationship with the pulse-width (equation 2.1). The output beam of OperaF is tunable over the wavelength range of 1,200 nm to 2,400 nm through a nonlinear optical parametric amplification. The bandwidth of the output beam varies across this tunable range due to the nonlinear nature of this conversion, so does it's transform-limited pulse-width. Moreover, as the laser beam travels through the different optical components of the microscope, the pulse picks up group delay dispersion (GDD) – the longer and the shorter wavelength parts of the pulse travel at a different speed, causing the pulse to spread spatially and reducing its efficacy for three-photon imaging.
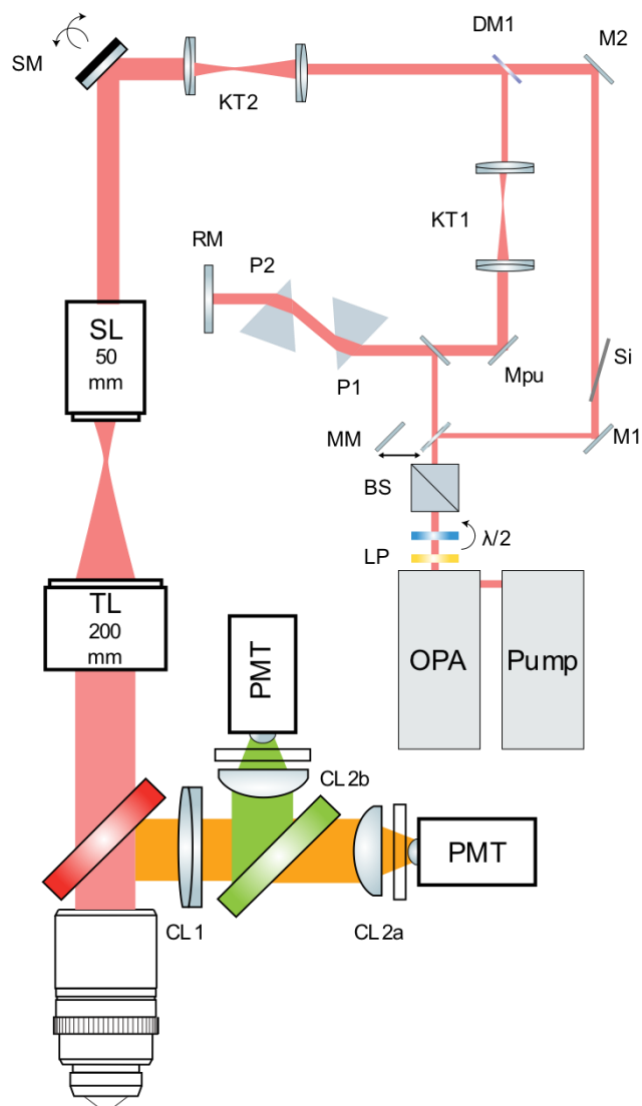
Figure 2.1 Three-photon movable microscope layout.

Schematic of three-photon microscope. LP: 1,200 nm long pass filter; λ/2: half-wave plate; BS: polarizing beamsplitter; MM: movable mirror; Mpu: pick up mirror; P1,P2: prism; RM: roof mirror; KT1,KT2: keplerian telescope; Si: silicon crystal; M1,M2: mirror; SM: scan mirror; SL: scan lens; TL: tube lens.

2.3.1 Pre-chirping the 1,320 nm beam

Positively dispersed beam (1,320 nm beam) can be pre-chirped for anomalous dispersion by either a prism or grating-based unit (Young, Field, Sheetz, Bartels, & Squier, 2015) to restore the transform-limited pulse-width. Here we are using a pair of prisms to pre-chirp the 1,320 nm beam. In this pre-chirp unit, longer wavelength part of the pulse takes a longer path across the prisms allowing the shorter wavelengths to catch up (Figure 2.2 A).

Following the attenuator, the beam is directed into the pre-chirp unit consisting of a pair of Brewster angle dispersing prisms (10SF10, Newport), a roof prism mirror (HRS1015-AG, Thorlabs) and a pick up D-mirror (PFD10-03-P01, Thorlabs). The prisms were initially placed at a distance of 54 cm based on the dispersion property of the microscope optics and later adjusted according to the pulse-width measurement.
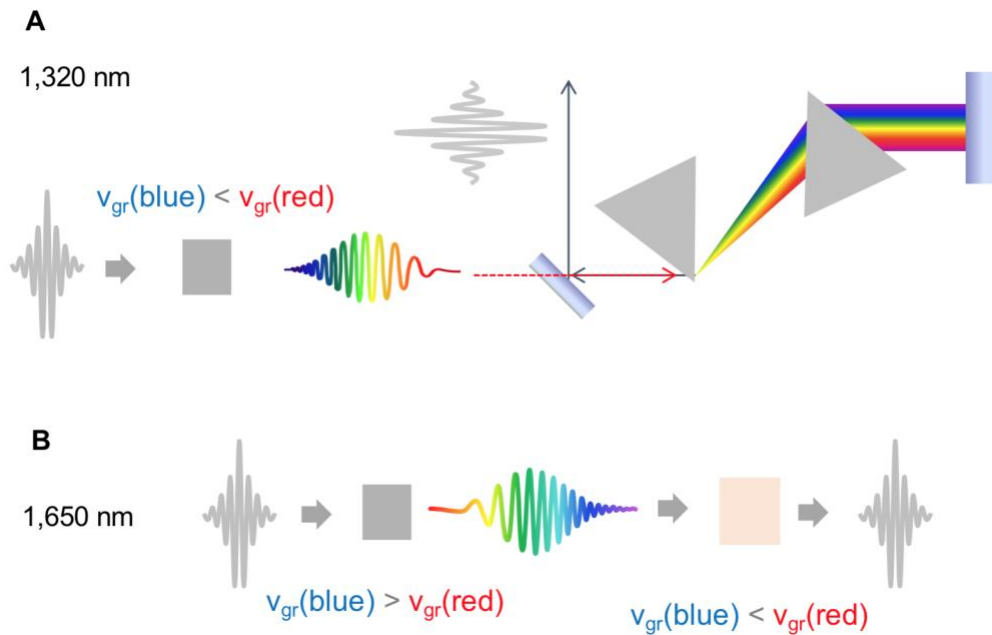

Figure 2.2 Dispersion compensation of excitation beam.

(A) Positive group delay dispersion of 1,320 nm excitation beam: longer wavelengths travel faster. A prism-pair compressor restores the pulse-width. (B) Negative group delay dispersion

of 1,650 nm excitation beam: shorter wavelength travel faster. Pulse-width restored by passing through material showing positive dispersion.

2.3.2 Pre-chirping the 1,650 nm beam

The 1,650 nm beam suffers from anomalous dispersion form the typical glass inside a microscope (Horton & Xu, 2015; Rasskazov et al., 2017). A few materials, however, show positive dispersion in this wavelength range, including silicon and zinc selenide (ZnSe). At 1,650 nm, the group delay dispersion (GVD) for Si and ZnSe are 3843 fs_2/mm and 356 fs_2/mm, respectively (Horton & Xu, 2015). Inlaying in the light path of the 1,650 nm beam with such crystals, can thus compensate for the pulse broadening by anomalous dispersion. Here we pre-chirp the 1,650 nm beam with a 3 mm thick silicon wafer (Edmund optics, # 68-523), placed at the Brewster angle (74°) and fine-tuned the pulse-width by either a 3 mm or 5 mm ZnSe crystal.

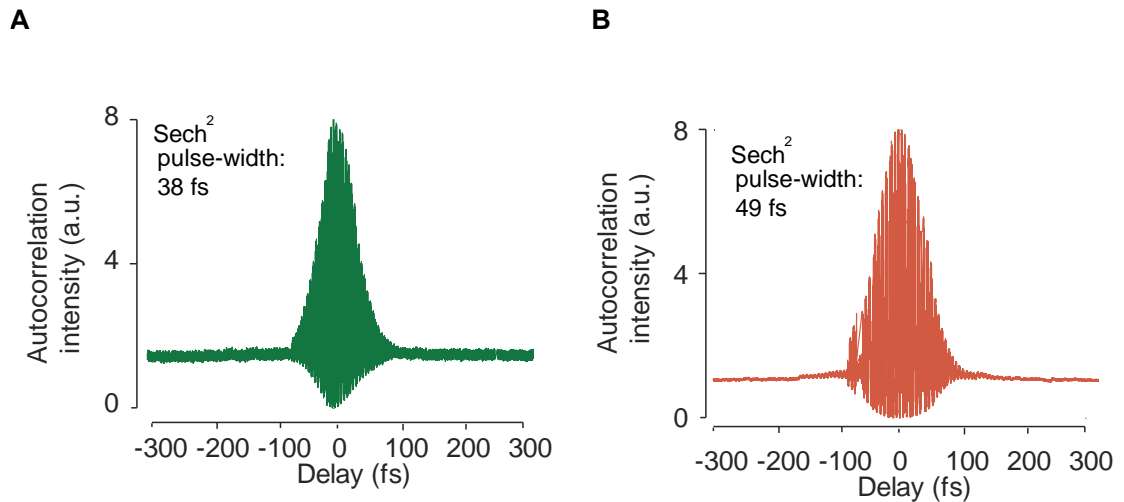**A**   **B**

Figure 2.3 Second-order autocorrelation trace of dispersion compensated pulse.

(A-B) Autocorrelation trace of dispersion compensated excitation by (A) prism compressor (1,320 nm) and (B) Si and ZnSe (1,650 nm).

2.4   Second-order autocorrelator for pulse characterization

We constructed an interferometric second-order autocorrelator (Armstrong, 1967) to characterize the laser beam. The second-order autocorrelator consists of a 45:55 pellicle beamsplitter (BP145B3, Thorlabs), a pair of mirrors, one of which was mounted on a piezo translator (PD72Z4CA0 and E-709, Physik Instrumente) and a Si photodetector (PDA100A, Thorlabs). The Si photodetector serves as both a nonlinear element and a slow detector—recording two-photon induced signal. During pulse-width measurement, the excitation beam is diverted to the autocorrelator through a series of flip mirrors. The interference signal is recorded at the focal plane of the microscope by modulating the piezo-actuated interferometer arm. The interferogram is digitized by NI USB DAQ-6008 and analyzed in MATLAB for $sech_2$ pulse-width. With the pre-chirp modules in place, the pulse-width at 1,320 nm and 1,650 nm is registered as 38 fs and 49 fs, respectively (Figure 2.3). These pulse-widths are close to the transform-limits, estimated from the spectral bandwidth (λ = 1,320 nm, $\Delta\lambda$ = 54 nm, transform-limited $sech_2$ pulse-width = 34 fs and λ = 1,650 nm, $\Delta\lambda$ = 62 nm, transform-limited $sech_2$ pulse-width = 46 fs) and also apparent from the autocorrelator traces, devoid of any sidebands.

2.5   Improved epi-collection of fluorescence and THG signal

Compared to confocal imaging, multiphoton microscopy is less susceptible to scattering. Longer wavelength excitation light is less prone to scattering (Helmchen & Denk, 2005) and optical sectioning by nonlinear confinement allows multiphoton microscopes to collect a larger fraction of the scattered photons on to a large-area detector that are typically rejected by the pinhole of a confocal microscope (Winfried Denk, 1996). However, in a turbid sample, the number of ballistic photons (unscattered) reaching the focus decreases exponentially with depth (Dunn, Wallace, Coleno, Berns, & Tromberg, 2000). So does the multiphoton absorption and photon emission. As a result, in a homogeneous turbid tissue, characterized by the

scattering length l_s, the depth-dependent fluorescence signal generation per fluorophore per unit time, $F_{gen}(z)$, can be represented as:

$$F_{gen}(z) \approx \eta \frac{\sigma}{\tau^{n-1}R^2}\left(\frac{NA^2}{2\hbar c\lambda}\right)^n \langle P \rangle^n e^{-nz/l_s} \qquad ...(2.2)$$

The blue-shifted emission, typically of the visible wavelength, suffers relative higher scattering on its way out of the sample. Photons arriving only within the acceptance angle are collected by the objective. A portion of this light, collected by the objective, is detected by the photosensor. Better detection of the emission signal allows imaging at a fixed signal to noise ratio (SNR) with reduced excitation. Compared to two-photon excitation microscopy, three-photon excitation microscopy requires a considerably higher energy pulse. Without efficient detection, three-photon microscopy runs the risk of photodamaging the sample by linear processes, principally heating (resulting from the absorption of infrared light by water in tissue) and non-linear processes (Koester, Baur, Uhl, & Hell, 1999).

As the resolution and discrimination are defined by the excitation process in a multi-photon microscope, a high numerical aperture (large acceptance angle) and low magnification objective with a large front element is favored for higher efficiency photon collection (Oheim, Beaurepaire, Chaigneau, Mertz, & Charpak, 2001). The collected photons at the objective back aperture (OBA) of one such a high NA, low magnification objective (XLUMPLFLN 20XW, NA 0.95, Olympus) have an angular distribution spanning divergent angles of larger than 11.5° (Zinter & Levene, 2011) and the photon distribution becomes increasingly uniform with scattering. The angular distribution of photons for a 25× NA 1.05 objective (XLPLN25XWMP2), used in our microscope, is expected to be similar if not spanning to even larger angles. When the scattering property of the sample is known, the exact distribution of the photons at the objective back aperture can be evaluated through Monte Carlo simulation (Oheim et al., 2001; Zinter & Levene, 2011). However, there is a limited body of literature on the optical properties

16

of fly brain tissue. A recent study has demonstrated air-filled tracheal network, distributed throughout the fly brain, makes the living brain of a fly is significantly more scattering than the mouse cortex (Hsu, Lin, Chiang, & Chu, 2019). Moreover, scattering property of the intermediate tissues such as the cuticle, adipose tissue, trachea and the air sacs in a transcutical brain imaging preparation is yet to be characterized. Nevertheless, given the substantial difference in refractive index among these intermediate layers (e.g., n=1 for the air inside the trachea and air sacs, n≃1.44 for the adipose tissue), photons in a transcutical brain imaging preparation would encounter significant scattering. Thus it is a reasonable zeroth-order approximation that the spatial distribution of photons reaching the objective's front aperture in is roughly uniform and their angular distribution is isotropic.

The wide angular distribution of the photons at the objective back aperture requires a high fidelity optical system to guides the photons onto the photocathode of a PMT, especially given that PMTs with high quantum efficiencies typically have small photocathodes, usually on the order of tens of square millimeters and a small numerical aperture. PMTs used in this study (H11706-40 and H10770B-40, Hamamatsu Photonics) have an active surface area of 19.6 mm2 and an acceptance angle of 38°.

Different optical design schemes have been explored to optimize photon collection onto the photodetector, including placing the detector close to the objective (Oheim et al., 2001), increasing the etendue of the detector by adding a field lens with index matching fluid onto the detector surface (Sofroniew, Flickinger, King, & Svoboda, 2016) and using large aperture optics 2" or 3" (Sofroniew et al., 2016; Tsai et al., 2015; Zinter & Levene, 2011) to minimize vignetting of highly scattered rays. The latter strategy has become more widespread in recent years, though it often requires custom optics.

Here we set out to maximize the collection etendue from the objective onto the PMT photocathode in an epi-collection configuration within the physical constraints of the Sutter MOM frame and those of the GaAsP PMT [H11706-40 and H10770B-40, Hamamatsu Photonics], using off-the-shelf optical components. It is a well-known fact that the effective field of view of a microscope objective is much larger than the field of view specified by the manufacturer, so is the objective back aperture (OBA). Given the ambiguity in the size and location of the OBA (manufacturer specifies the approximate location of OBA), we developed our analysis around the objective rear element (ORE), with a measured clear aperture diameter of 20 mm.

The etendue at the objective rear element, e, expressed as $e = \int dS \cdot d\mathbb{W}$, where $\mathbb{W}$ is the angular distribution (field angle) of the photons and dS is the differential area of objective rear element. For a uniform spatial distribution of photons across the aperture of area A, the etendue is simply, $e = A\int d\mathbb{W}$. As photons travel through the optics, a portion of the light is vignetted by the limiting apertures. Thus, the fraction of photon collected by the photocathode is $e_{col} = A\int v(\mathbb{W}) \cdot d\mathbb{W}$, where $v(\mathbb{W})$ is the fraction of unvignetted light. Here we optimize our design for the figure of merit defined as $e_{fom} = \int v(\mathbb{W}) \cdot d\mathbb{W}$.

From the objective rear element to the PMT photocathode, the optomechanics (3D geometry) of the light path is modeled in Zemax and the system is analyzed for the wavelength of 550 nm. All calculations neglect reflective losses from the Fresnel reflections at optical interfaces. Based on ray-tracking, the fraction of unvignetted light reaching the photocathode is evaluated, and subsequently, the figure of merit e_{fom} is assessed.
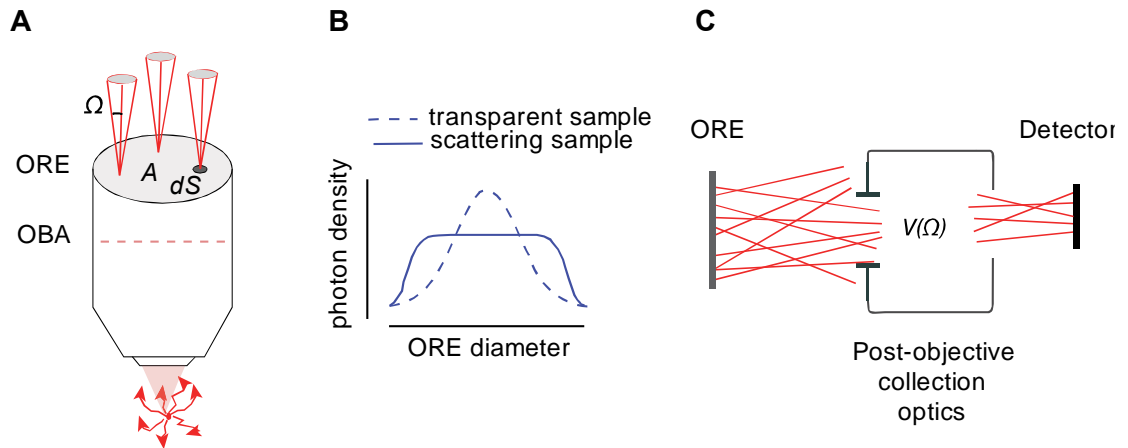
Figure 2.4 Post-objective photon collection.

(A-B) Distribution of photons collected by a high NA, low magnification objective. OBA: objective back aperture, ORE: objective rear element. (C) Photons traveling at different angles from the ORE to the detector encounter different vignetting factor.

First, we evaluated the performance of the Sutter PMT assembly with this scheme. PMT assembly consisting of a 22 x 29 mm primary dichroic, a 150 mm plano-convex (Edmund optics #47-643) and an 18 mm aspheric (G317704000, Linos) collection lens (CL1 and CL2), a secondary dichroic (Di02-R488-25 × 36, Semrock) and an emission filter (ET525/70m-2p, Chroma). An short-pass laser blocking filter is also incorporated in this analysis. Figure 2.5 shows representative ray diagram and corresponding the vignetting is plot. This analysis revealed a couple of areas for improvement. First, with a relatively large focal length, the converging power of CL1 is limiting the photon collection. Second, a large fraction of the light, travelling at large angles, is vignetting at the primary dichroic and CL1.
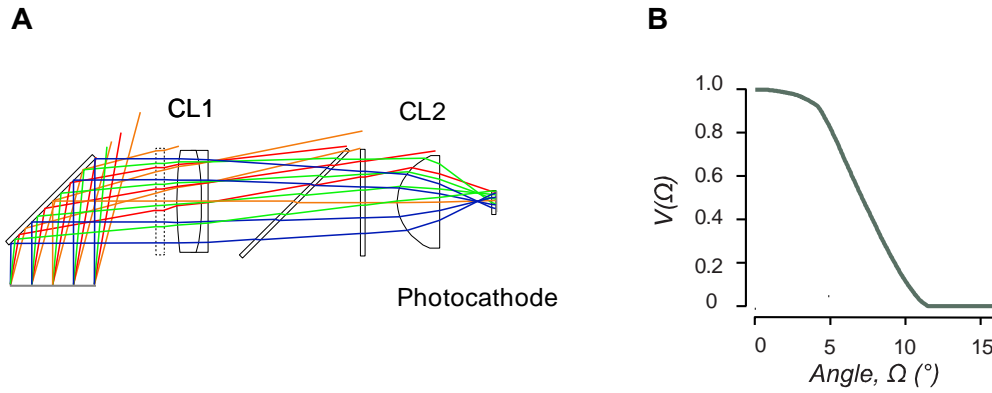
A

B

Figure 2.5 Ray-tracing and vignette analysis of the former design.

(A) Representative ray diagram of the former design from ORE to the photocathode. CL1: f= 150 mm, CL2 f =18 mm. (B) Fraction of unvignetted photons as a function of Ω.

A

B

C

CL1	φ 25 mm	φ 30 mm
150 mm	7.1614	7.2856
100 mm	7.9817	8.3469
75 mm	8.762	9.6028
50 mm	10.1734	11.8244

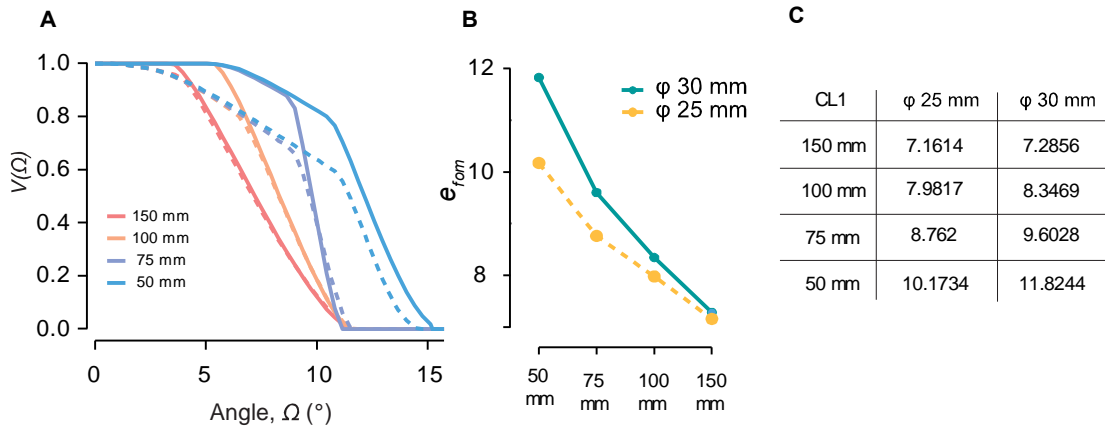Figure 2.6 Collection efficiency improves with focusing power and aperture.

(A) Fraction of unvignetted photons for different CL1 focal length. Solid line: CL1 diameter 30 mm . dashed line: CL1 diameter 25 mm. (B) Collection figure of merit for combinations of focal length and CL1 and primary dichroic aperture size. (C) List of figure of merit values for combinations of focal lengths and aperture sizes.

Next, we analyzed the impact of the focal length and the aperture size of CL1 by placing an observation plane immediately after to the CL2. We limit the choice of focal lengths and the optics size to off-the-shelf components and to confer with the mechanical design of the microscope frame. We also increased the size of the primary dichroic from 22 x 29 mm to a standard 1" dichroic (25 x 36 mm). Results are summarized in Figure 2.6. It is clear from the vignetting diagram (Figure 2.6 A) that shortening the focal length of CL1 to 50 mm significantly increases the collection of photons travelling beyond 10° and enlarging the aperture of primary dichroic and CL1 raise the fraction of photons collected at a given angle.
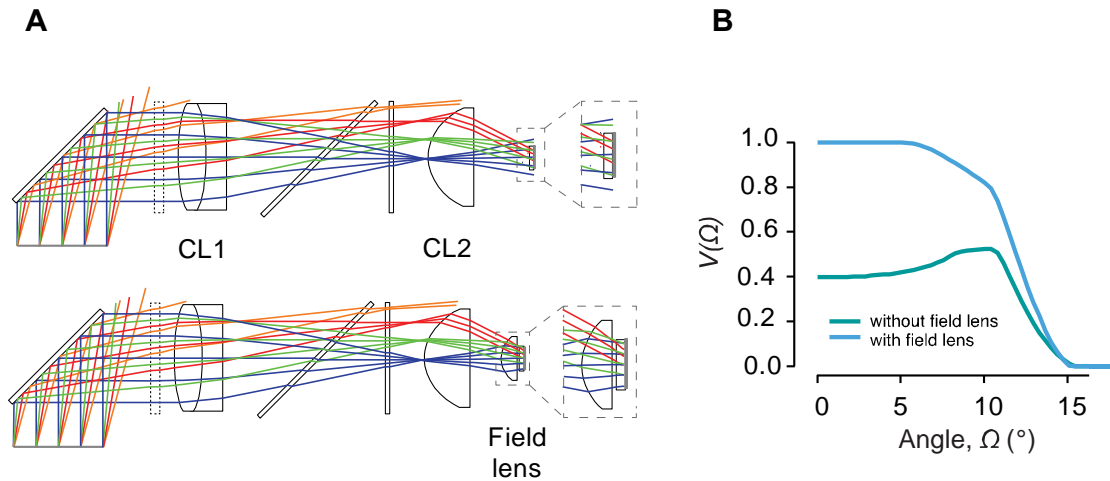

Figure 2.7 Collection efficiency improved by field lens.

(A) Ray diagram with and without field lens. Field lens increases acceptance angle of the detector and improves collection efficiency. (B) Fraction of unvignetted photons with and without field lens.

However, due to limiting aperture (acceptance angle) of the PMT photocathode, much of this improvement is not translated in actual collection by the detector (Figure 2.7). This shortcoming was resolved by introducing a field lens (A240-A, Thorlabs) adjacent to the photocathode (Liu, Li, Marvin, & Kleinfeld, 2019; Sofroniew et al., 2016) and optimizing the spacing between the CL2 and the field lens.
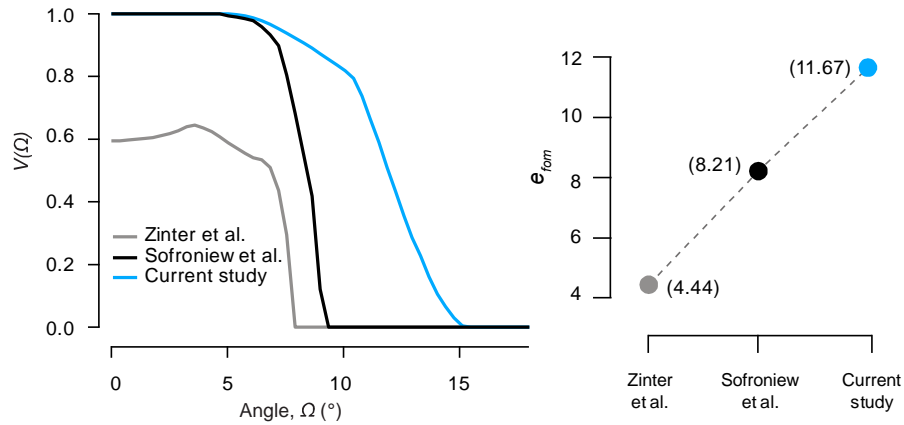

Figure 2.8 Efficiency comparison of different study.

(A) Fraction of unvignetted photons in post-objective collection optics design proposed in different studies. (B) The collection figure of merit of different designs.

Following this analysis, we compared the performance of our design with the ones put forward by Zinter et al. 2011 and Sofroniew et al. 2016. The study by Zinter et al. emphasizes on the use of large aperture optics by deploying a custom-made 40 mm x 57 mm primary dichroic and 40 mm diameter optics. However, our analysis reveals that the collection efficiency is severely limited by the limiting aperture of the PMT used in that study (H7422P-40mod, Hamamatsu Photonics). Sofroniew et al. employed both large aperture optics and a tailor-made field lens to the sensor window through index matching fluid to expand the acceptance angle of the detector. Nevertheless, this design is plagued by the sizable optical distance from the

objective to the detector, inevitably vignetting all light traveling at angles beyond 9°. In contrast, our design with a compact layout, collects photons traveling up to 13° with efficiencies upwards of 30%.
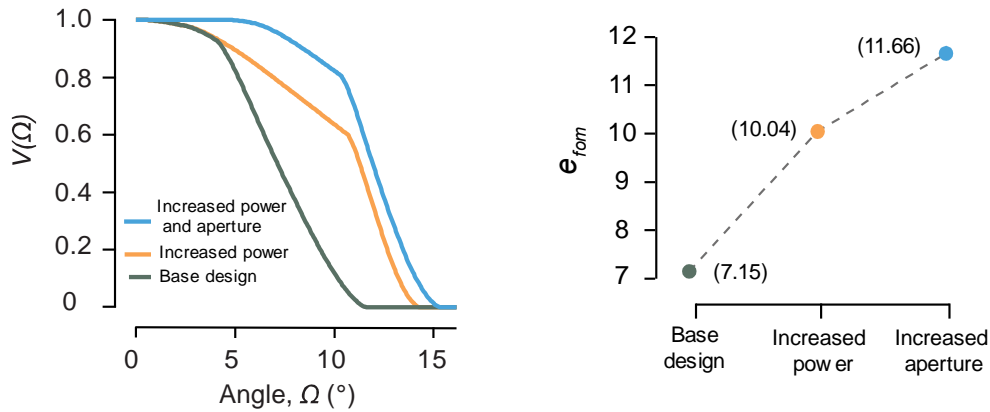

Figure 2.9 Impact of lens power and aperture on efficiency.

(A-B) Fraction of unvignetted photons and collection figure of merit for optical design with increased power and increased aperture size.

2.6   Epi-collection detector performance characterization

Next, we analyzed the impact of the two key efficiency improving attributes of our design: the enhanced converging power of the collection lens 1 (CL1) and the increased aperture size of the collection optics by means of imaging a tissue phantom (details of the tissue phantom is discussed in method). We compared three post-objective collection configurations: (i) the former design (Figure 2.5), (ii) CL1 replaced with a shorter focal length lens (f=50 mm, dia = 25 mm, Edmund #47-637) and (iii) increased aperture size of the primary dichroic (T735LPXRXT-25 × 36, Chroma) and CL1 (f=50 mm, dia = 30 mm, Edmund #47-713). A field lens (A240-A, Thorlabs) was added to the configuration (ii) and (iii) to exclude the impact of vignetting by the PMT aperture. The ray-tracing analysis, with the underlying assumption of

uniform photon distribution, predicts an improvement in collection efficiency over the former design by 40% in the configuration (ii) and 63% in the configuration (iii) (Figure 2.9). In contrast, measurements from the tissue phantom revealed an improvement of 43% and 91% on the surface by enhanced converging power of the CL1 and increased aperture of epi-collection, respectively (figure 2.10 A). Moreover, the fluorescent collection improvement increased monotonously with the imaging depth, indicating increased scattering at greater depths. Subsequently, we imaged a fly brain embedded in agarose with a pan-neuronal expression of GFP (*elav*>CD8GFP) and observed an average improvement of 74% for the proposed optimum epi-collection design (iii) (Figure 2.10 B).
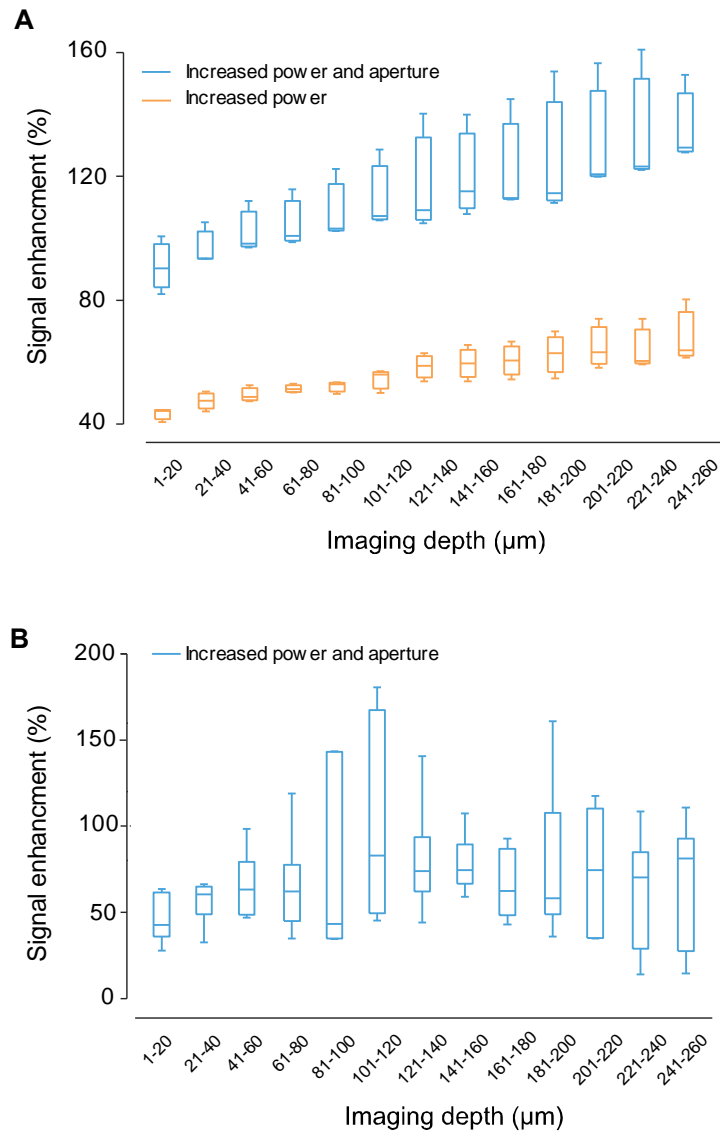
Figure 2.10 Characterization of epi-collection detector.

(A) Signal detection enhancement characterized by imaging tissue phantom. (B) Signal detection enhancement characterized by imaging fly brain embedded in agarose. Boxplot with maximum, minimum, third quartile, first quartile and mean (A: n=3, B: n=5).

2.7   Method

2.7.1   Tissue phantom preparation

Yellow-green fluorescent sulfate microspheres with an average diameter of 20 nm (F8845, Thermo Fisher), was used as a reporter, intralipid 20% (I141, Sigma Aldrich) as a scattering medium and agarose as gel matrix for the imaging phantom. The phantom was created with a mixture of intralipid, agarose and fluorescent microspheres of 4%, 0.5% and 0.17%, respectively, diluted in deionized water. To ensure a flat and optically transparent imaging surface, a 500 µm deep imaging chambers were constructed with #1 coverslips and imaging chamber gasket (Thermo Fisher C18160).

2.7.2   *ex vivo* fly brain preparation

Female flies, 7 days old, expressing GFP under the pan-neuronal driver *elav-Gal4* were used for imaging experiments. The adult brain was dissected in Ca_{2+} free AHL saline and embedded with 1% agarose gel (Sigma, type VII-A) in AHL saline warmed to 37°C and placed on a #1 coverslip in a dorsal to ventral orientation for imaging.

2.7.3   Imaging and analysis

The tissue phantom and the fly brain were imaged on at 1,320 nm excitation with an average laser power of 6 mW. Images were registered for a depth of 0 – 260 µm in 5 µm increments and a resolution of 128 x 128 pixels (205 x 205 nm for each pixel). To ensure accurate determination of the sample surface, scans were initiated approximately 25 µm above the sample surface and the image with the maximum average pixel value was defined as depth $z = 0$. Images were analyzed in MATLAB with the average pixel value of the entire field of view of the phantom and average of top 0.1% brightest pixels for the fly brain, taken as the signal and binned over a 20 µm depths for collection efficiency analysis.

3   Visualization of Neuromodulation of Fly Brain Circuit by a Gut-derived Hormone

The nervous system integrates external stimuli and internal states such as motivation, arousal, drive or emotion to drive adaptive behavior. Hormones and neuromodulators encode internal states and exert influence by modulating or reconfiguring neuronal circuits to shape animal behavior. Recent studies have revealed novel mechanisms linking the gut-brain axis to behavior and emotions (Dinan & Cryan, 2017).

In *Drosophila* males, we have found ingested amino acids (AA) promote mating drive. Following a series of behavior-genetic, we identified two key sites of action in the fly gut and brain, required for this aphrodisiac effect. AA ingestion activates diuretic hormone 31 (Dh31) releasing enteroednocrine cells in the gut and a subset of the Dh31 receptor (Dh31R) expressing neurons in the brain release corazonin to modulate the dopamine tone of a central hub for courtship (Lin at el., unpublished).

Gut to brain communication can be mediated by vagal afferent neurons or circulating hormones or both (Berthoud, 2008). Compared to vagal transmission, hormones can broadcast the signal to different organs for functional coordination. *Drosophila* has afferent and efferent nerves connecting the gut and brain (Cognigni, Bailey, & Miguel-Aliaga, 2011). However, more studies are needed to reveal their functional relevance.

Using non-invasive imaging, here we visualize the neuromodulation of corazonin neurons in the fly brain by a gut-derived signaling and probe the mode of communication for this gut to brain communication.

3.1 Corazonin neurons show evoked response to circulatory Dh31 hormone

Dh31 is co-expressed in the enteroednocrine cells with other neuropeptides, including Tachykinin, Neuropeptide F and CCHamide-1a (Guo et al., 2019). We investigated if corazonin neurons in the central brain are specifically responding to the gut-derived Dh31 by first monitoring their response to circulating Dh31.

For all the experiments described in this chapter, we expressed either jRCaMP1b or GCaMP7s (Dana et al., 2016, 2019) calcium reporter in corazonin neurons and imaged through the cuticle. Under CO_2 anesthesia, flies were mounted onto the edge of a glass coverglass at the posterior side of their head. UV light was then used to cure the glue for 5 seconds. For imaging, the coverglass was mounted on a custom fly holder and deuterated water was used as the emersion medium to minimize heat generation from the absorption of infrared light by water.

We injected 10 µM Dh31 synesthetic peptide diluted in sugar-free AHL saline (J. W. Wang, Wong, Flores, Vosshall, & Axel, 2003) into the dorsal heart chamber with a sharp glass pipette. We observed that corazonin neurons in the brain exhibited robust calcium activity in response (Figure 3.1 C) to Dh31 injection. Notably, there was a latency of few minutes from the time of injection to a sharp increase in the calcium activity (Figure 3.1 D).

A 3P Imaging

Dh31

B

C

100%

5 min

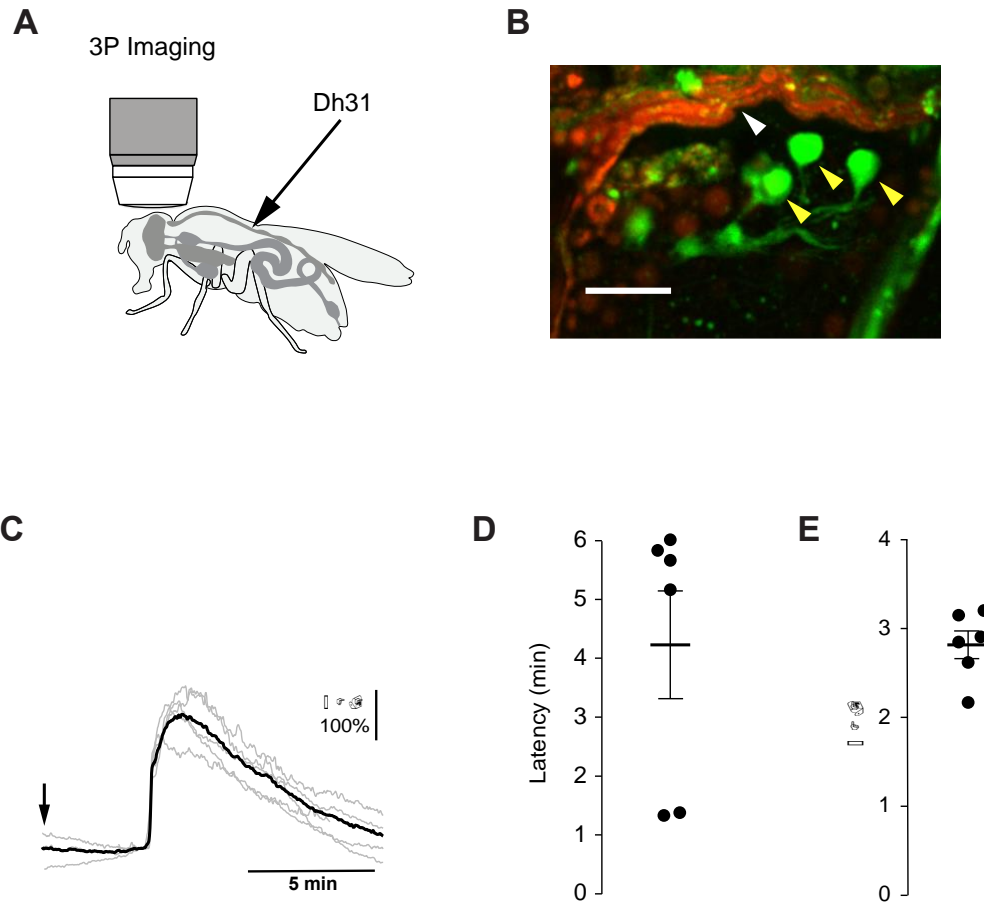**D**

Latency (min)

E

Figure 3.1 Circulatory Dh31 hormone elicits calcium activity in corazonin neurons.

(A) Three-photon imaging of corazonin neurons in the brain while Dh31 peptide was injected into the dorsal heart chamber. (B) A representative image showing three-photon fluorescence signals in green and third-harmonic signals in red. Scale bar, 25 μm. White arrow: cuticle; yellow arrows: corazonin neurons. (C) Corazonin neuron response to injected Dh31 peptide, arrow indicate the time of injection. (D-E) Latency (D) and ΔF/F (E) of corazonin neurons in response injected Dh31 peptide.

3.2 Corazonin neurons show evoked response to Dh31 released from the enteroendocrine cells

Next we excited the Dh31+ enteroendocrine cells by optogenetic stimulation and imaged the corazonin neurons in the brain to identify the dynamics of this aphrodisiac neuromodulation. We expressed CsCrimson (Klapoetke et al., 2014) in Dh31+ enteroednocrine cells. Flies were raised with standard corn food with a 0.4 mM retinal supplement for 7 days from eclosion to imaging experiments but were deprived of food for one day before imaging. A piece of black aluminum foil was used to block the fly head from the optogenetic stimulation. Images were acquired at 0.5 frames/s, and interleaved by 800-ms optogenetic stimulation (660 nm).

We found that the corazonin neurons in the brain exhibited robust calcium activity in response to light activation of the Dh31+ enteroednocrine cells (Figure 3.2 B). Notably, the response latency decreased from 18 to 3 minutes with an increasing light stimulation intensity (Figure 3.2 C), whereas the peak $\Delta F/F$ did not change with stimulation intensity (Figure 3.2 D). Flies raised with food without retinal supplements did not show calcium activity in response to optogenetic stimulation (data not presented here).
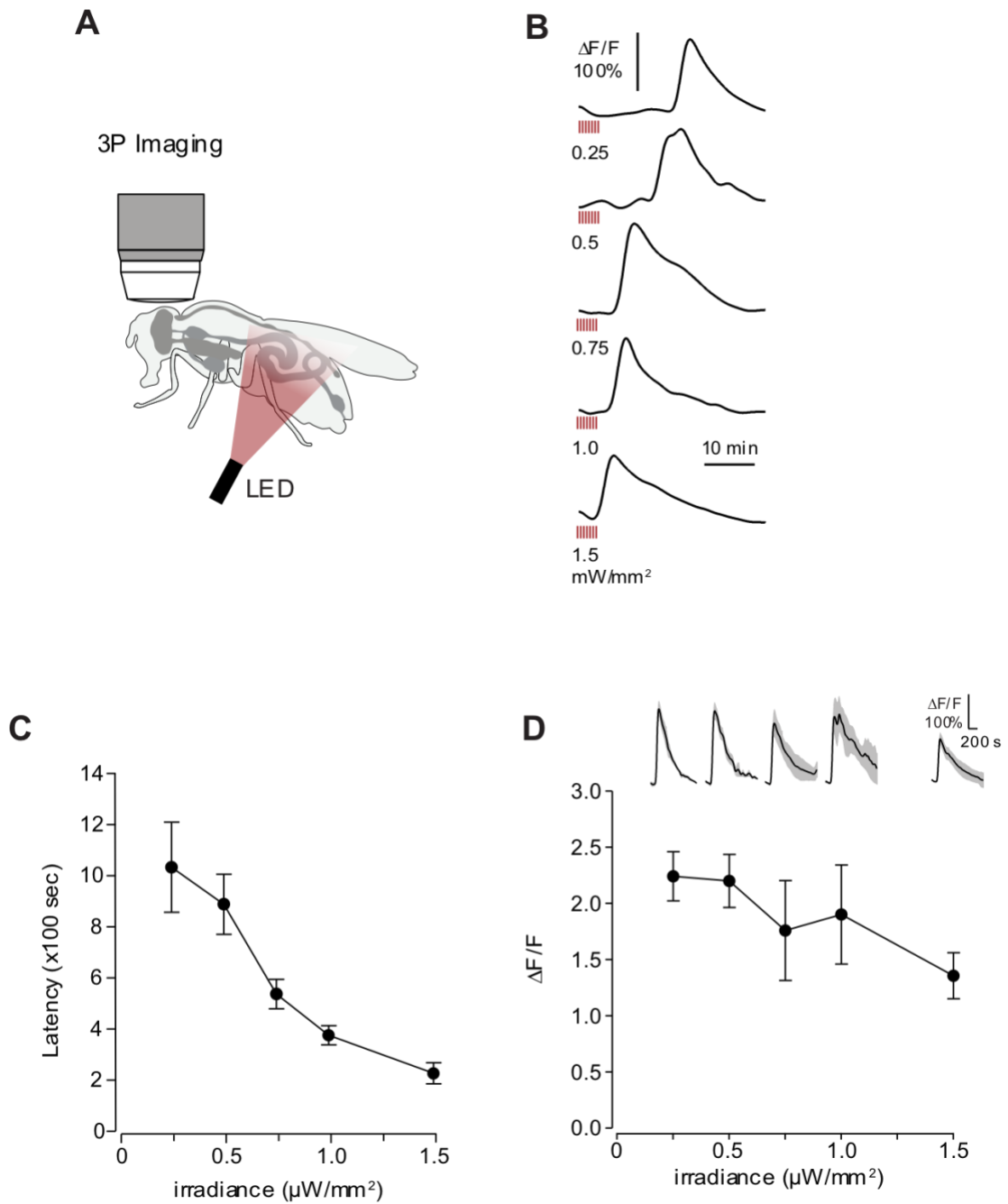
Figure 3.2 Gut-derived Dh31 elicits calcium activity in corazonin neurons.

(A) Three-photon microscopy was used to image corazonin neurons in the brain while Dh31 enteroendocrine cells were optogenetically stimulated. (B) Representative ΔF/F traces of

corazonin neurons in response to optogenetic activation of Dh31+ enteroendocrine cells at stimulation intensity ranging from 0.25 to 1.5 mW/mm2 (C-D) Latency (C) and ∆F/F (D) of corazonin neurons Inset shows average ∆F/F traces aligned by the rising phase of each trace.

3.3 Neuromodulation of Corazonin neurons by gut-derived Dh31 acts through the circulation

Based on the latency observed in the response of corazonin neurons from the previous two experiments, we hypothesized that the neuromodulation is acting through the circulation, To test this hypothesis, we perturbed the circulation. We reasoned that a cardiac arrest should retard the circulation, thereby increasing the response latency of the Dh31R+ corazonin neurons in the brain. Brief exposure to CO_2 has been shown to cause cardiac arrest in flies (Badre, Martin, & Cooper, 2005). To calibrate the effect of CO_2 exposure on the cardiac function, we used fluorescence microscopy to monitor the diameter of the heart-tube in male flies that express tdTomato in cardiomyocytes (Klassen et al., 2017). Our measurements indicated that flooding the imaging chamber with CO_2 stopped the heart briefly and it took about 5 min for the heartbeat frequency to return to the normal level.

We observed an increase of the response latency of the Dh31R+ corazonin neurons by about 7 min when the light activation of Dh31 enteroednocrine cells occurred under the influence of CO_2 (Figure 5E). Again, ∆F/F was not changed by CO_2 exposure (Figure 5F). Taken together, our imaging results suggest that Dh31 release from enteroednocrine cells activates corazonin neurons in the brain through the circulatory system.
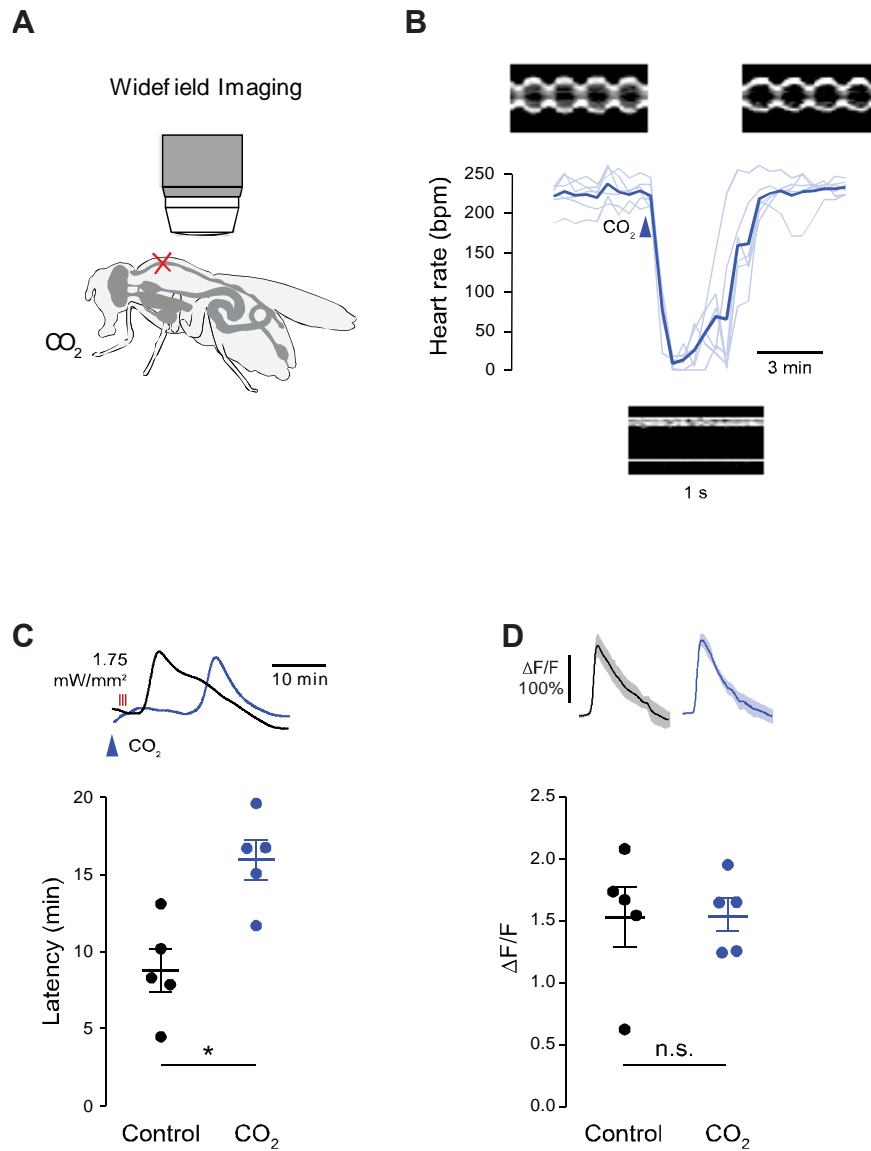
Figure 3.3 Cardiac arrest retard corazonin neurons response to gut-derived Dh31.

(A) Exposure to CO_2 induce cardiac arrest. (B) Effect of CO_2 exposure on heartbeat frequency. Images show the changing diameter of the heart-tube in male flies expressing tdTomato in cardiomyocytes. Data was from 6 males. (C-D) The effect of CO_2-induced cardiac arrest on the response latency (C) and peak $\Delta F/F$ (D) of corazonin neurons in response to optogenetic activation of Dh31 enteroendocrine cells. Stimulation intensity: 1.75 mW/mm$_2$. *, $p < 0.05$, n = 6, t-test.

3.4   Remarks

Through non-invasive imaging and simultaneous optogenetic stimulation, we have visualized the neuromodulation of a courtship promoting brain circuit by a gut-derived neuropeptide. Furthermore, we have shown perturbing the circulation by cardiac arrest retards the response of the corazonin neurons, indicating the neuromodulator (Dh31) acts through the circulation. Future experiments would be necessary to determine the mechanisms by which the neuromodulator (Dh31) crosses the blood-brain barrier.

Bibliography

Barad, Y. *et al.* (1997) 'Nonlinear scanning laser microscopy by third harmonic generation', *Applied Physics Letters*, 70(8), pp. 922–924. doi: 10.1063/1.118442.

Denk, W., Strickler, J. and Webb, W. (1990) 'Two-photon laser scanning fluorescence microscopy', *Science*, 248(4951), pp. 73–76. doi: 10.1126/science.2321027.

Freund, I. and Deutsch, M. (1986) 'Second-harmonic microscopy of biological tissue', *Optics Letters*, 11(2), p. 94. doi: 10.1364/OL.11.000094.

Hell, S. W. (1996) 'Three-photon excitation in fluorescence microscopy', *Journal of Biomedical Optics*, 1(1), p. 71. doi: 10.1117/12.229062.

Helmchen, F. and Denk, W. (2005) 'Deep tissue two-photon microscopy', *Nature Methods*. Nature Publishing Group, 2(12), pp. 932–940. doi: 10.1038/nmeth818.

Horton, N. G. *et al.* (2013) 'In vivo three-photon microscopy of subcortical structures within an intact mouse brain', *Nature Photonics*. Nature Publishing Group, 7(3), pp. 205–209. doi: 10.1038/nphoton.2012.336.

Hsu, K.-J. *et al.* (no date) 'Whole-brain imaging and characterization of Drosophila 1 brains based on one-, two-, and three-photon excitations 2 3'. doi: 10.1101/339531.

Huang, C. *et al.* (2018) 'Long-term optical brain imaging in live adult fruit flies', *Nature Communications*. Nature Publishing Group, 9(1), p. 872. doi: 10.1038/s41467-018-02873-1.

Kobat, D. *et al.* (2009) 'Deep tissue multiphoton microscopy using longer wavelength excitation.', *Optics express*, 17(16), pp. 13354–64. doi: 10.1364/oe.17.013354.

Kobat, D., Horton, N. G. and Xu, C. (2011) 'In vivo two-photon microscopy to 1.6-mm depth in mouse cortex.', *Journal of biomedical optics*, 16(10), p. 106014. doi: 10.1117/1.3646209.

Kou, L., Labrie, D. and Chylek, P. (1993) 'Refractive indices of water and ice in the 0.65- to 2.5-μm spectral range.', *Applied optics*, 32(19), pp. 3531–40. doi: 10.1364/AO.32.003531.

Takahara, Y., Matsuki, N. and Ikegaya, Y. (2011) 'Nipkow Confocal Imaging for Deep Brain Tissues', *Journal of Integrative Neuroscience*, 10(01), pp. 121–129. doi: 10.1142/S0219635211002658.

Theer, P. and Denk, W. (2006) 'On the fundamental imaging-depth limit in two-photon microscopy.', *Journal of the Optical Society of America. A, Optics, image science, and vision*, 23(12), pp. 3139–49. Available at: http://www.ncbi.nlm.nih.gov/pubmed/17106469.

Theer, P., Hasan, M. T. and Denk, W. (2003) 'Two-photon imaging to a depth of 1000 µm in living brains by use of a Ti:Al_2O_3 regenerative amplifier', *Optics Letters*, 28(12), p. 1022. doi: 10.1364/ol.28.001022.

Wang, M. *et al.* (2018) 'Comparing the effective attenuation lengths for long wavelength in vivo imaging of the mouse brain', *Biomedical Optics Express*. Optical Society of America, 9(8), p. 3534. doi: 10.1364/BOE.9.003534.

Wokosin, D. L. *et al.* (1996) 'Three-photon excitation fluorescence imaging of biological specimens using an all-solid-state laser', *Bioimaging*, 4(3), pp. 208–214. doi: 10.1002/1361-6374(199609)4:3<208::AID-BIO11>3.3.CO;2-A.

Xu, C. *et al.* (1996) 'Multiphoton fluorescence excitation: new spectral windows for biological nonlinear microscopy.', *Proceedings of the National Academy of Sciences*, 93(20), pp. 10763–10768. doi: 10.1073/pnas.93.20.10763.

Zipfel, W. R. *et al.* (2003) 'Live tissue intrinsic emission microscopy using multiphoton-excited native fluorescence and second harmonic generation', *Proceedings of the National Academy of Sciences*, 100(12), pp. 7075–7080. doi: 10.1073/pnas.0832308100.